Revealing Large-Scale Surface Subsidence in Jincheng City's Mining Clusters Using MT-InSAR and VMD-SSA-LSTM Time Series Prediction Model

Fan Yang
Liaoning Technical University
Menghui Zhi
Zhi_mh@163.com

Liaoning Technical University
Yan An
Liaoning Technical University

Article

Keywords: Surface Subsidence, MT-InSAR, VMD-SSA-LSTM, Driving force

Posted Date: June 7th, 2024

DOI: https://doi.org/10.21203/rs.3.rs-4474949/v1

Additional Declarations: No competing interests reported.

Version of Record: A version of this preprint was published at Scientific Reports on February 17th, 2025. See the published version at https://doi.org/10.1038/s41598-025-88524-0.

Revealing Large-Scale Surface Subsidence in Jincheng City's Mining Clusters Using MT-InSAR and VMD-SSA-LSTM Time Series Prediction Model

Yang Fan[1,2] , Menghui Zhi[1] , An Yan[1]
(1. School of Surveying, Mapping and Geoscience, Liaoning University of Engineering and Technology, Fuxin 123000;
2. Institute of Science and Technology, Liaoning University of Engineering and Technology, Fuxin 123000)

Abstract: Jincheng City's mining areas have long been plagued by surface subsidence, posing significant threats to local residents' safety and impacting the region's economic and social stability. Understanding and effectively monitoring the driving factors and mechanisms of surface subsidence are crucial for devising scientific prevention measures and promoting the sustainable development of mining areas. This article aims to comprehensively reveal the large-scale surface subsidence phenomenon in Jincheng City's mining clusters by utilizing advanced remote sensing technology and machine learning models, identifying its main driving forces, and predicting future subsidence trends to provide scientific evidence for geological disaster prevention in mining areas. The study employs Multi-Temporal Interferometric Synthetic Aperture Radar (MT-InSAR) technology, using both Permanent Scatterer Interferometric SAR (PS-InSAR) and Small Baseline Subset Interferometric SAR (SBAS-InSAR) techniques for cross-validation, to confirm the existence of surface subsidence. Further, by integrating Variational Mode Decomposition (VMD), Singular Spectrum Analysis (SSA), and Long Short-Term Memory (LSTM) networks, a high-precision time series prediction model (VMD-SSA-LSTM) was developed. The results indicate that from 2018 to 2021, the surface subsidence rates in Jincheng City ranged from -34 to 34 millimeters per year, with significant variations in subsidence levels across different areas. Gaoping City exhibited the highest subsidence, with rates ranging from -34 to 5 mm per year, while Yangcheng County showed the most pronounced subsidence changes. These variations are primarily attributed to mining activities, land use changes, and adverse geological conditions in Jincheng City. This study unveils the large-scale surface subsidence phenomenon in Jincheng City's mining clusters, marking the first comprehensive ground deformation monitoring analysis of small mining clusters across four cities in Jincheng. The development of a high-precision surface subsidence prediction model provides new insights for scientifically understanding geological disasters in mining areas. These findings are significant for formulating effective geological disaster prevention measures and land management policies.

Keywords: Surface Subsidence; MT-InSAR; VMD-SSA-LSTM; Driving force

Supported by the Key Laboratory of Land Satellite Remote Sensing Application, Ministry of Natural Resources (LSMNR-202107); and the Discipline Innovation Team of Liaoning University of Engineering and Technology (LN-TU20TD-27).

Corresponding author: Menghui Zhi, Research interests include homeland space and disaster monitoring, remote sensing data processing and InSAR monitoring, **E-mail:zhi_mh@163.com**

First author: Yang Fan , Professor, main research interests are deformation monitoring and forecasting theory, homeland space and disaster monitoring, remote sensing data processing and InSAR monitoring. e-mail: yangfan2008beijing@126.com

1 Introduction

Surface subsidence is a potential geological hazard resulting from the combined effects of natural processes and human activities[1]. Its severity has garnered widespread attention globally[2]. This phenomenon is particularly pronounced in mining regions[3,4]. Additionally, human activities such as groundwater extraction and national economic development have exacerbated the trend of surface subsidence[5]. Surface subsidence poses threats to the safety of infrastructure[6] and can severely impact the ecological environment[7,8] and socioeconomic stability[9]. Therefore, monitoring, analyzing, and predicting surface subsidence in mining areas are crucial for identifying potential geological hazards and ensuring their sustainable and stable development.

Traditional methods of monitoring surface subsidence, such as leveling surveys and Global Navigation Satellite Systems (GNSS), are limited by their low resolution, limited coverage, and high costs. In contrast, Interferometric Synthetic Aperture Radar (InSAR) technology, as a high-precision remote sensing monitoring method with high temporal and spatial resolution[10], can effectively measure large-scale ground deformation. InSAR compensates for the shortcomings of traditional methods and plays a key role in surface deformation monitoring. By utilizing the phase information of radar beams, InSAR can achieve centimeter- and even millimeter-level surface deformation monitoring[8,11].

PS-InSAR, one of the first techniques of MT-InSAR, aims to identify highly coherent Permanent Scatterers (PS) in urban areas[12,13]. However, in low-coherence areas, such as suburbs or mountainous regions, the application of PS-InSAR is limited due to the widespread presence of Distributed Scatterers (DS) such as pavements and vegetation. To address this issue, Distributed Scatterer Interferometric SAR (DS-InSAR) was proposed as the second generation of MT-InSAR[14,15]. Typical algorithms include SqueeSAR[16,17] and Small Baseline Subset (SBAS)[18,19]. Compared to SqueeSAR, SBAS has broader applicability and can handle various surface changes, including the complex geological conditions and diverse surface deformation mechanisms of mining areas. The SBAS algorithm processes large amounts of radar image data efficiently, enabling large-scale monitoring.

Jincheng City, the study area, is characterized by rich coal and mineral resources, frequent geological disasters[20], and significant socioeconomic status[21]. Surface subsidence caused by coal mining and other activities has become increasingly prominent, impacting the local environment, infrastructure, and residents' safety[22]. Therefore, in-depth research on surface subsidence in Jincheng City is essential for understanding the mechanisms of geological disasters in mining areas, maintaining local economic and social stability, and promoting sustainable development[23,24].

InSAR technology has been applied to subsidence monitoring in mining areas, usually using InSAR technology alone for monitoring. However, studies on large-scale cluster mining areas are relatively few. In this study, we take Jincheng City, China, as an example and use a novel method combining MT-InSAR[25,26] technology and LSTM [27,28]neural networks to monitor and analyze mining area subsidence. We aim to reveal the surface subsidence phenomenon in large-scale mining clusters. Cross-validation of PS-InSAR and SBAS-InSAR results confirmed the existence of surface subsidence, and we used an LSTM model to predict subsidence. Through time series deformation analysis, we explored the main driving forces and mechanisms of surface subsidence.

2 Study Area and Data Set

2.1 Study Area

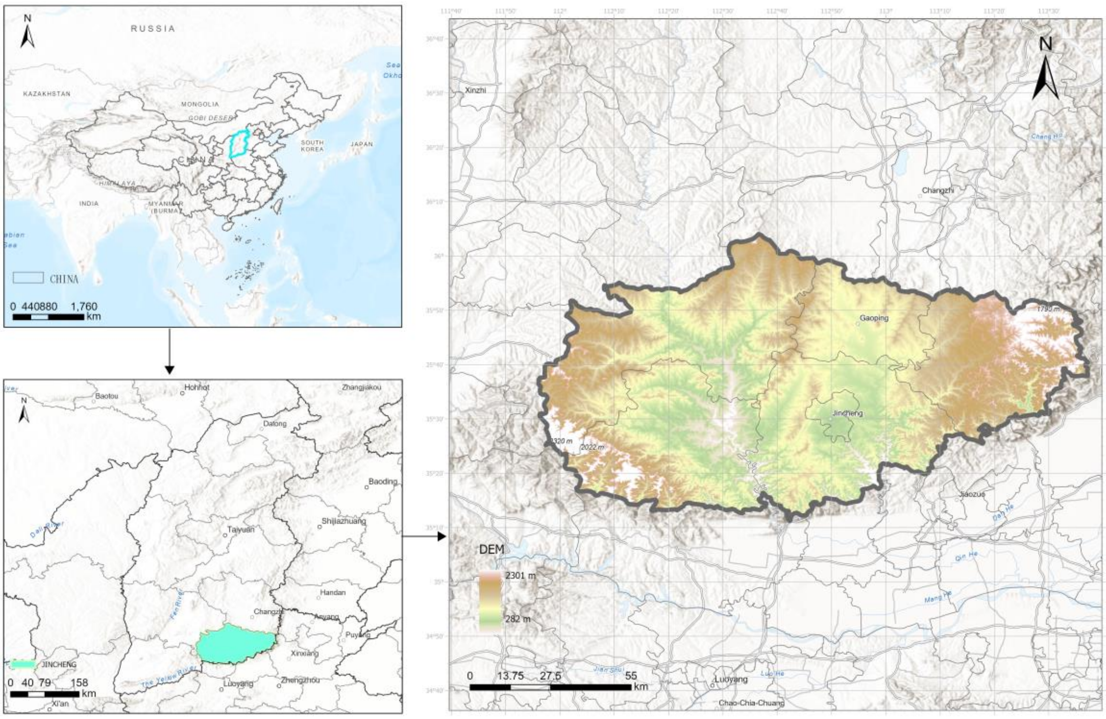

Figure 1. Geographical location of Jincheng City

Jincheng City ,as shown in Figure 1,is located in the central part of Shanxi Province, China, situated at the eastern edge of the Shanxi Basin, between latitudes 35°29′ to 36°37′ N and longitudes 111°20′ to 113°09′ E. The city covers an area of approximately 8,569 square kilometers. The topography is predominantly low hilly terrain with gentle undulations, and elevations range from 400 to 1,000 meters. This topographical feature significantly influences the city's natural environment and urban planning. Additionally, Jincheng City, located at the eastern edge of the Shanxi Basin, has complex geological structures with various lithologies and structural forms. Rich in coal resources, it has become an important coal industry base in China, making Jincheng a significant coal resource city. Numerous coal mines are distributed in and around the city, forming a prosperous coal industry. The coal industry is a pillar of the city's economy, playing a crucial role in local economic development and social stability. However, long-term coal mining activities have led to widespread surface subsidence in mining areas, posing significant challenges to the local environment, infrastructure, and residents' safety and well-being. Therefore, in-depth research on surface subsidence in mining areas is of great practical significance and scientific value.

2.2 Data Sets

2.2.1 SAR Data

Sentinel-1 SAR Data: The Sentinel-1 SAR data used in this study is provided by the European Space Agency (ESA) and can be accessed through ESA's Sentinel data access portal (https://scihub.copernicus.eu/). The data covers the period from January 1, 2018, to December 28, 2020, comprising a total of 81 scenes. It is acquired in single polarization mode (VV polarization) and provided in Single Look Complex (SLC) format, featuring high spatial and temporal resolution suitable for surface deformation monitoring and analysis.

2.2.2 Multi-Source Auxiliary Data for Studying Factors Influencing Surface Subsidence

Digital Elevation Model (DEM) Data: The DEM data used is the Shuttle Radar Topography Mission 1-second resolution (SRTM1) Digital Elevation Model (DEM) provided by NASA. This data can be accessed via the USGS EarthExplorer portal (https://earthexplorer.usgs.gov/). The SRTM1 data offers high spatial resolution and global coverage, providing essential baseline information for the study area's topographical characteristics.

Global Atmospheric Correction Service (GACOS) Data: The GACOS data, used for atmospheric correction of SAR interferometry data to eliminate atmospheric effects on surface deformation monitoring, is available from the European Space Agency's website (https://earth.esa.int/web/guest/-/gacos-for-sentinel-1).

Precise Orbit Data: Precise orbit data can be obtained from the International Earth Rotation and Reference Systems Service (IERS) website (https://www.iers.org/IERS/EN/DataProducts/EarthOrientationData/eop.html). This data provides accurate satellite orbit information, crucial for precise geolocation and correction of SAR images, thereby enhancing the accuracy of surface deformation monitoring.

Land Use Data: The land use/cover data set, provided by Professor Yang Jie's team from Wuhan University, is accessible through the research paper "30m annual land cover and its dynamics in China from 1990 to 2019" published in Earth System Science Data.

3 Methodology

3.1 Time Series InSAR (TS-InSAR) Analysis

TS-InSAR is a surface deformation monitoring technique based on multi-temporal SAR images. By utilizing multiple temporal SAR interferograms, it enables high-precision monitoring and analysis of surface deformation [7,29]. The principle relies on the coherence of SAR technology and multi-temporal data overlay analysis. In this study, the SBAS-InSAR method is selected for analysis.

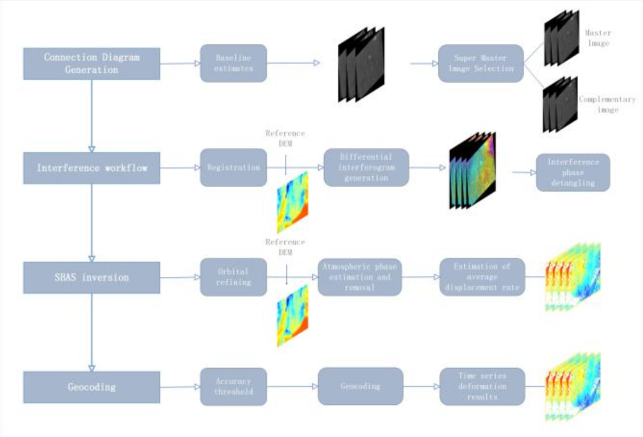

Figure 2. TS-InSAR Technical Process

Figure 2 illustrates the process of monitoring surface deformation using the SBAS-InSAR approach. The core principle involves selecting SAR image pairs with short temporal and spatial baselines to perform differential interferometry and obtain surface deformation information. The basic principle of SBAS-InSAR is as follows[19,30]:

Assume two SAR images acquired at times t_A and t_B . For a pixel (x, y) in the images, the differential interferometric phase $\delta\Phi(x, y)$ can be expressed as:

$$\delta\Phi(x,y) = \Phi(t_B, x, y) - \Phi(t_A, x, y) \tag{1}$$

where $\delta\Phi(x, y)$ and $\Phi(t_A, x, y)$ are the interferometric phases of the pixel at times t_A and t_B , respectively.

Based on the basic principles of radar interferometry, the relationship between surface deformation $d(x, y)$ and differential interferometric phase $\delta\Phi(x, y)$ can be expressed as:

$$\delta\Phi(x,y) = \frac{4\pi}{\lambda} \cdot d(x,y) \cdot \sin\theta \tag{2}$$

where $\lambda$is the radar wavelength, and θ is the radar beam's incidence angle. This formula establishes the mathematical relationship between surface deformation and differential interferometric phase.

The key to the SBAS-InSAR method is selecting SAR image pairs with short temporal and spatial baselines for differential interferometry. By setting appropriate temporal and spatial baseline thresholds, eligible image pairs can be selected, and differential interferograms generated. Subsequently, techniques such as multi-look processing and phase unwrapping are used to extract high-coherence pixels and invert surface deformation information.

3.2 Land Use Change

The land use transition matrix reveals the mutual conversion of various land use types within a specific period. This matrix is presented in a square format, with rows and columns representing different land use types. Each element in the matrix represents the area or percentage of conversion from one land use type to another. The matrix not only shows the quantity of land use type changes but also reveals trends and patterns in land use change by comparing transition matrices at different time points[29].Expression:

$$S = \begin{bmatrix} S_{11} & \cdots & S_{1i} & \cdots & S_{1n} \\ \vdots & \ddots & \vdots & \ddots & \vdots \\ S_{i1} & \cdots & S_{ij} & \cdots & S_{in} \\ \vdots & \ddots & \vdots & \ddots & \vdots \\ S_{n1} & \cdots & S_{nj} & \cdots & S_{nn} \end{bmatrix} \tag{4}$$

where S is the transition matrix within the study period, S_{ij} represents the area (km^2) of land use/land cover type i converting to type j within the study period, and n is the number of land use/land cover types.

Chord diagrams (also known as Sankey diagrams or energy flow diagrams) play an important role in land use change analysis.

Chord diagrams graphically display the energy flow or conversion relationships between different land use types. In chord diagrams, different land use types are represented as nodes, and the lines between nodes represent the flow of energy or area, i.e., land use type conversion. The thickness and length of the lines indicate the rate or quantity of conversion. Chord diagrams visually demonstrate the complex conversion relationships between land use types, aiding in understanding the dynamic processes of land use change.

3.3 Multivariate Neural Network Prediction Model

The VMD-SSA-LSTM time prediction model combines the advantages of VMD, SSA, and LSTM techniques. It decomposes the original data using VMD, optimizes the LSTM model using SSA, and finally uses LSTM for prediction[27,30]. This combined model exhibits high prediction accuracy and flexibility in handling complex time series data. The three components are introduced below:

Variational Mode Decomposition (VMD): VMD is a signal processing technique used to decompose complex time series signals into multiple intrinsic mode functions (IMFs)[31,32]. These modes reflect different frequency components and amplitude variations within the signal. Compared to traditional decomposition methods like Empirical Mode Decomposition (EMD), VMD better adapts to non-linear and non-stationary signals and has superior local feature extraction capabilities. Through VMD, the original time series data is decomposed into multiple IMF components and residual components.

Sparrow Search Algorithm (SSA): SSA is an optimization algorithm typically used to search for the optimal parameters[33]. In this model, SSA may be used to optimize the parameters of the LSTM or other prediction models to improve prediction accuracy.

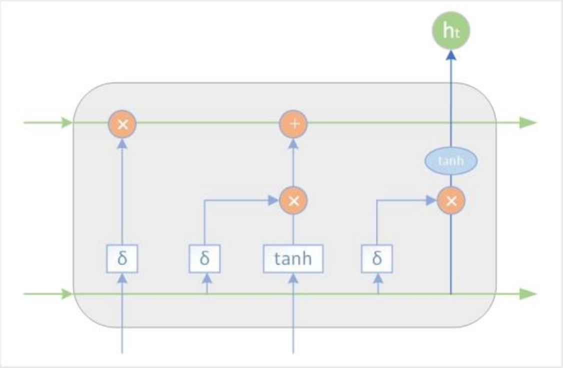

Figure 3. Basic Structure of the LSTM Model

Figure 3 illustrates the basic structure of the LSTM model.Long Short-Term Memory (LSTM): LSTM is a specialized type of Recurrent Neural Network (RNN) [34]designed to handle time series data. It introduces gating mechanisms (such as forget gates, input gates, and output gates) to address the issues of gradient vanishing and gradient explosion in traditional RNNs[27,35].

Input Gate: Controls the extent to which new information enters the cell state:

$$i_t = \sigma(W_i \cdot [h_{t-1}, x_t] + b_i) \tag{5}$$

Where x_t is the current input, h_{t-1} is the hidden state from the previous time step, Wi is the weight matrix of the input gate,bi is the bias vector of the input gate, and σ is the sigmoid activation function, compressing output values to the [0, 1] range.

Forget Gate: Determines the extent to which old information is forgotten in the cell state:

$$f_t = \sigma\left(W_f \cdot [h_{t-1}, x_t] + b_f\right) \tag{6}$$

Candidate Memory Cell: Generates new candidate memory values, processed by the tanh activation function, determining which new information is added to the cell state:

$$\tilde{C}_t = \tanh(W_C \cdot [h_{t-1}, x_t] + b_C) \tag{7}$$

Cell State: The core of the LSTM, representing the storage of cell memory, updated as follows:

$$C_t = f_t \cdot C_{t-1} + i_t \cdot \tilde{C}_t \tag{8}$$

where f_t decides how much of the old memory C_{t-1} is retained, and i_t decides how much of the new memory C_t is added.

For each IMF component and residual component, a separate LSTM model can be established for prediction.

4. Results Analysis

4.1 Validation of interferometric synthetic aperture radar ground settlement results

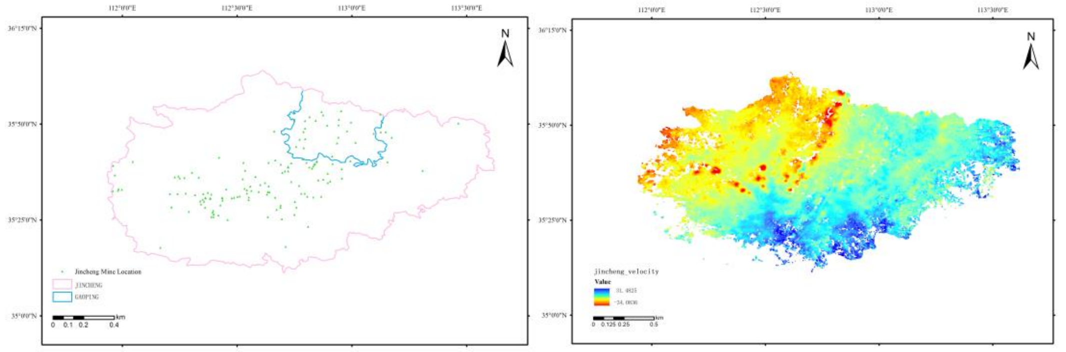

Figure 4. InSAR Cross-Validation and Mining Area Data Map

Figure 4 presents the distribution map of mining areas in Jincheng City, created using the 2021 version of the national mineral distribution data downloaded from the National Geological Archives of China (left). To ensure the accuracy of the data, we excluded non-operational and closed mines, retaining only the active mining areas. The right image displays the average subsidence rate map for Jincheng City. By comparing the distribution map of mining areas in Jincheng City with the InSAR subsidence rate map, a high degree of consistency between the two can be clearly observed.

First, there is a consistency in spatial distribution: the mineral distribution map shows the specific locations and extents of the main mining clusters in Jincheng City, while the InSAR subsidence rate map reveals obvious signs of subsidence in these areas. Second, there is a correlation between subsidence rates and mining activity intensity: areas with higher subsidence rates on the InSAR subsidence rate map often correspond to areas with frequent mining activities or intensive mining operations on the mineral distribution map.

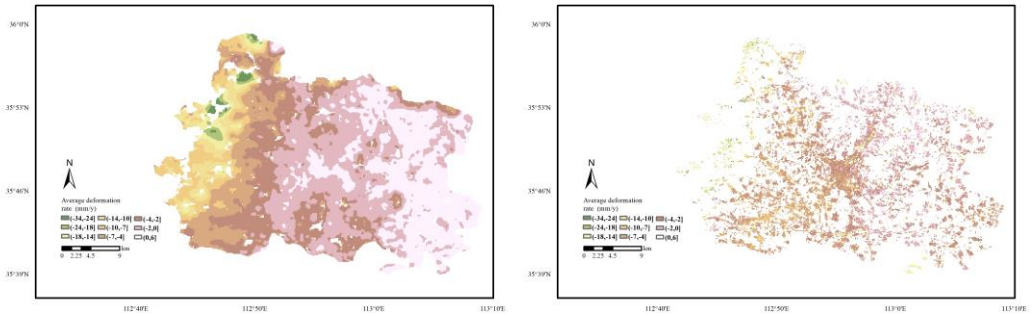

Figure 5. Comparison of SBAS-InSAR and PS-InSAR Subsidence Rates in Gaoping City

Figure 5 compares the average subsidence rate maps of Gaoping City obtained using PS-InSAR and SBAS-InSAR methods. The detected subsidence areas are highly consistent between the two methods, showing similar distribution characteristics of higher subsidence rates. Notably, significant subsidence phenomena are detected in the northwest and southwest parts of Gaoping City by both methods, indicating that the western region is the main subsidence area. The overall trend is consistent, suggesting that these areas may experience strong mining activities or other geological events causing ground subsidence.

On the basis of consistent overall spatial distribution, the specific subsidence rate values also show good agreement. The subsidence rate values obtained by PS-InSAR and SBAS-InSAR methods are similar in most areas, further proving the reliability of both methods in monitoring ground subsidence.

4.2 Overall Deformation of Mining Area Clusters

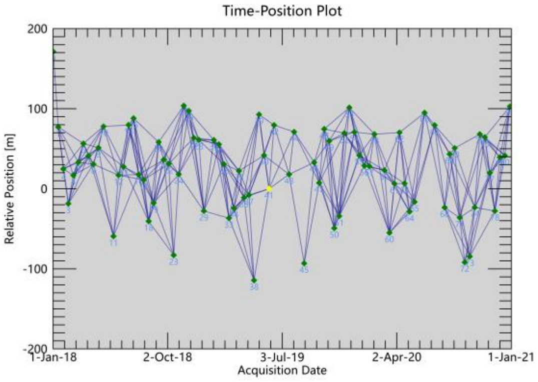

Figure 6. Spatial-temporal baselines configuration of the generated interferograms.

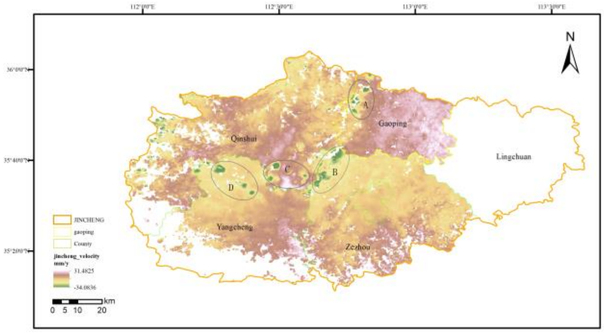

Figure 7. the overall average deformation rate in Jincheng City.

Based on the principles of generating connection graphs, 326 interferogram pairs were generated, as shown in Figure 6, the temporal and spatial baseline configuration of the generated interferograms, with the yellow point representing the reference image (20190601). Subsequently, we used the synthetic aperture radar interferometry method to study the ground deformation of mining clusters in Jincheng City. We extracted ground deformation data from January 1, 2018, to January 1, 2021, covering multiple small mining clusters. As shown in Figure 7, detailed analysis reveals that the average deformation rate ranges from -34.08 mm/year to 31.48 mm/year. The green areas represent the most significant subsidence phenomena, with subsidence points mainly distributed in the northwest of Gaoping City, the northwest corner of Zezhou County, and the northern part of Qinyuan County. These concentrated subsidence points connect to form a large mining cluster in Jincheng City, showing a linear high-density distribution along the borders of various counties. Compared to the mining cluster areas, most other regions exhibit relatively mild surface deformation trends, particularly in the central Qinyuan County, central Gaoping City, and most parts of Zezhou County. It should be noted that due to coherence loss, parts of the northern and southern edges of the study area in Jincheng City were not included in further analysis.

4.3 Regional Mining Area Subsidence Deformation

4.3.1 Small Mining Area Clusters in Gaoping City

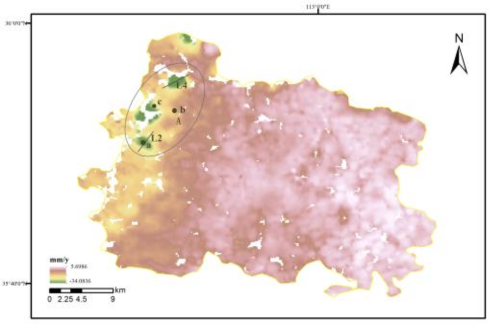

Figure 8. the average deformation rate in Gaoping City.

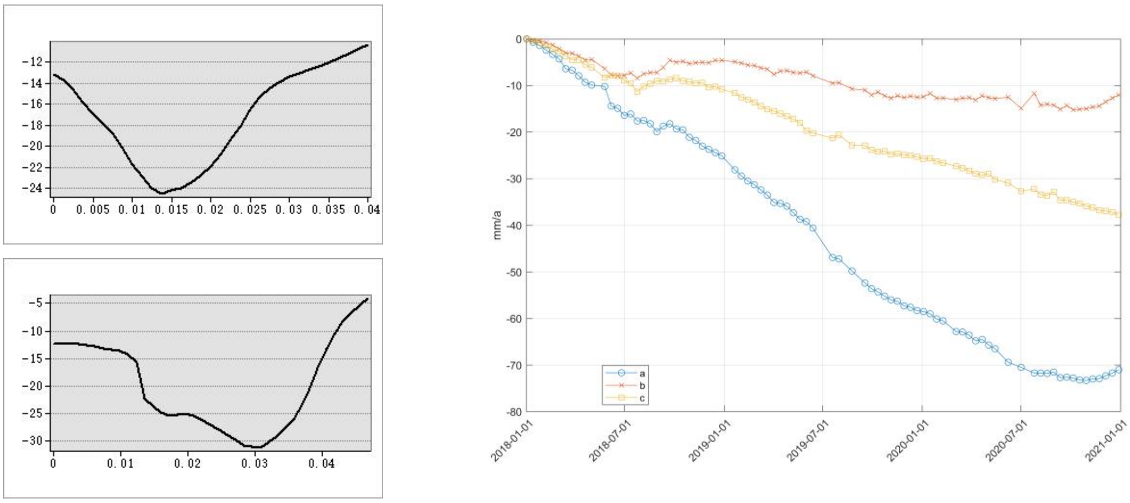

Figure 9: The two left images are cross-sectional analysis charts of average subsidence rates in two regions of Gaoping City. The horizontal axis represents distance in degrees, and the vertical axis represents subsidence rate in mm/year(same below). The upper left represents L2(Region 2), and the lower left represents L4(Region 4). The right side shows the subsidence time series curves for randomly selected points in the Figure.

As shown in Figure 9,The 3D cross-sectional data of subsidence in Region 2 shows a funnel-shaped subsidence pattern, consistent with the characteristics of mining subsidence, where the subsidence rate is linearly related to the distance from the mining center. as shown in Figure 8, the subsidence map of Gaoping City, it can be observed that at the outermost distance, the initial value is -13.11 mm/year, reaching a minimum of -24.51 mm/year at 0.01 degrees, then gradually recovering to -10.34 mm/year at 0.04 degrees. The subsidence rate decreases from -13.11 mm/year to -24.51 mm/year, indicating significant variation within this interval, possibly due to the influence of underground structures and mining activities. Subsequently, the subsidence rate gradually recovers, suggesting that the geological conditions in this area may become stable, reducing subsidence impacts.

For Region 4, the cross-sectional analysis shows that its subsidence rate varies significantly over time. The initial value is -12.32 mm/year, reaching a minimum of -31.08 mm/year at 0.027 degrees, then gradually recovering to -4.09 mm/year at 0.047 degrees. The subsidence rate decreases from -12.32 mm/year to -31.08 mm/year, indicating significant variation within this interval, possibly closely related to underground mining activities.

For the spatiotemporal subsidence values in Gaoping City from January 1, 2018, to January 1, 2021, three typical points were selected for analysis. As shown in the Figure, the subsidence at the three mining points exhibits different trends: point a shows the most significant subsidence, dropping from 0 mm to about -71 mm, with an accelerated subsidence after mid-2019; point b is relatively stable, dropping from 0 mm to about -12 mm, showing a gradual subsidence trend; point c's subsidence lies between the two, dropping from 0 mm to about -37 mm, with a significant increase in subsidence rate after mid-2019. Overall, point a has the most severe subsidence, point b is the mildest, and point c is intermediate.

4.3.2 Small Mining Area Clusters in Zezhou County

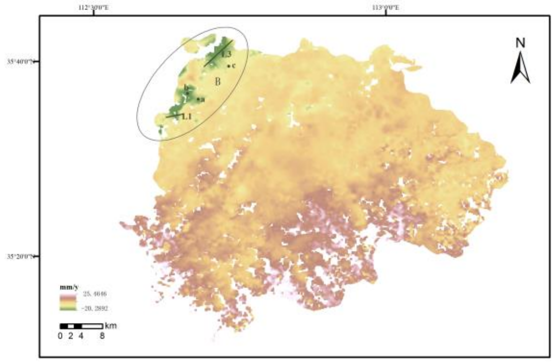

Figure 10 the average deformation rate in Zezhou County.

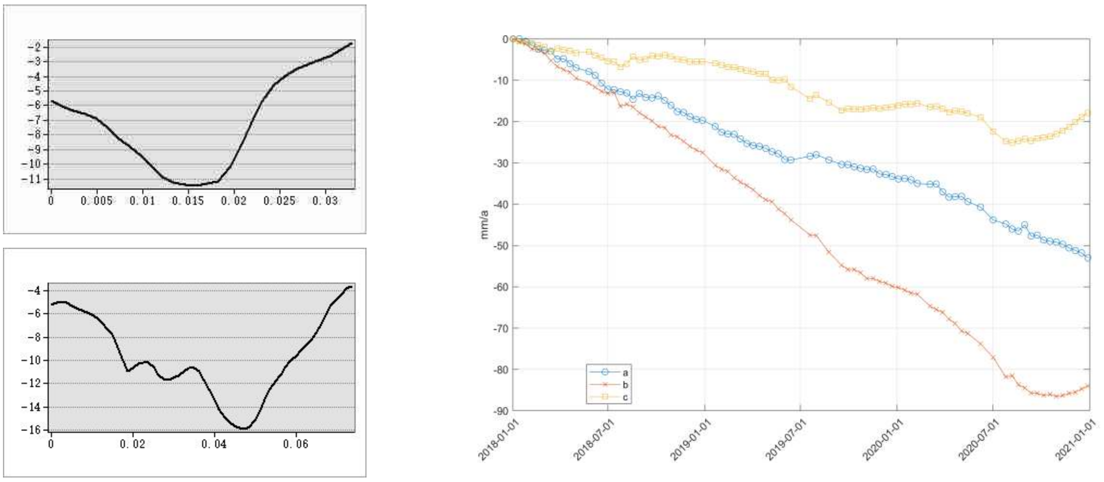

Figure 11: The upper left represents L1(Region 1), and the lower left represents L3(Region 3). The right side shows the subsidence time series curves for randomly selected points.

As shown in Figure 10, both areas in Zezhou County are part of small mining clusters. As shown in Figure 11, The cross-sectional analysis of Region 1 shows a funnel-shaped subsidence pattern, with higher subsidence rates towards the central part and more stable conditions towards the edges, with almost no subsidence at the boundaries. Region 3, however, shows a nonlinear subsidence trend, with subsidence rates varying with distance, peaking at -16 mm at 0.05 degrees. According to the subsidence rate map of Zezhou County, this variation might be due to the mining clusters not existing as independent mining areas.

From January 1, 2018, to January 1, 2021, the subsidence data for the three monitoring points (a, b, c) in the small mining area clusters of Zezhou County show a clear subsidence trend, with significant differences in subsidence magnitude and rate among the points. Monitoring point b shows the most severe subsidence, dropping from 0 mm to about -84 mm, with a notable increase in subsidence rate after mid-2019. Monitoring point a also shows significant subsidence, dropping from 0 mm to about -53 mm, with an accelerated subsidence rate after 2020. Monitoring point c shows the least subsidence, dropping from 0 mm to about -18 mm, but its subsidence rate also increases after 2020. Overall, monitoring point b shows the most severe subsidence, followed by point a, and point c shows relatively mild subsidence, indicating significant spatial differences in subsidence within the area. Further monitoring and mitigation measures are needed for areas with severe subsidence.

4.3.3 Small Mining Area Clusters in Qinyuan County

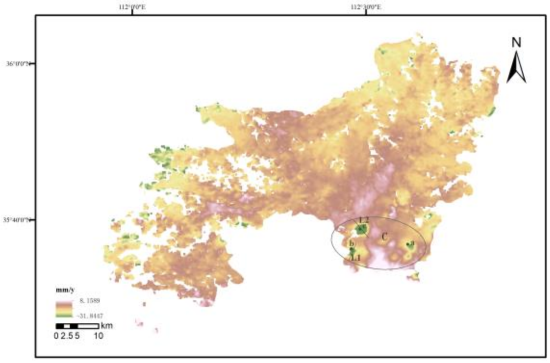

Figure 12 shows the average deformation rate in Qinyuan County.

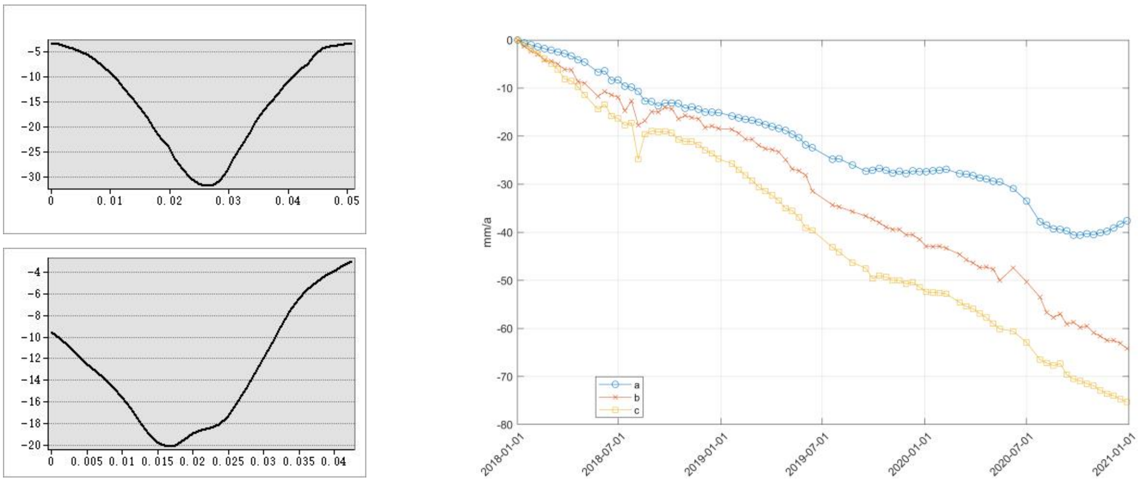

Figure 13: The upper left represents L1, and the lower left represents L2. The right side shows the subsidence time series curves for randomly selected points.

In Figure 12, Qinyuan County, both regions 1 and 2 show a similar trend in subsidence, initially increasing and then decreasing, both showing a funnel shape. However, As shown in Figure 13,the maximum subsidence rate for Region 1 is 30 mm/year, whereas for Region 2 it is only 20 mm/year. Analyzing the subsidence rate map, the difference in subsidence rates might be due to different mining times and geological structures.

The ground subsidence in the small mining area clusters of Qinyuan County is analyzed using monitoring data from three points (a, b, c). The data show varying degrees of subsidence at each point, all showing a significant downward trend. Initially, point a shows slight subsidence, gradually dropping from 0 mm to about -8.11 mm, accelerating to -28.11 mm in the mid-term, and reaching a maximum of -37.6 mm in the later period. Point b's subsidence rate accelerates in the mid-term, dropping from -6.11 mm to -39.11 mm, and finally to -64.21 mm. Point c shows the most severe subsidence, dropping from -8.11 mm initially to -39.11 mm in the mid-term, and finally to -75.31 mm. This significant subsidence indicates that underground mining activities may have caused substantial changes in the geological structure, necessitating further monitoring and mitigation measures to prevent geological disasters.

4.3.4 Small Mining Area Clusters in Yangcheng County

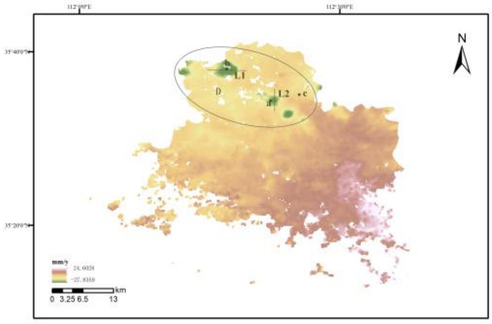

Figure 14 shows the average deformation rate in Yangcheng County.

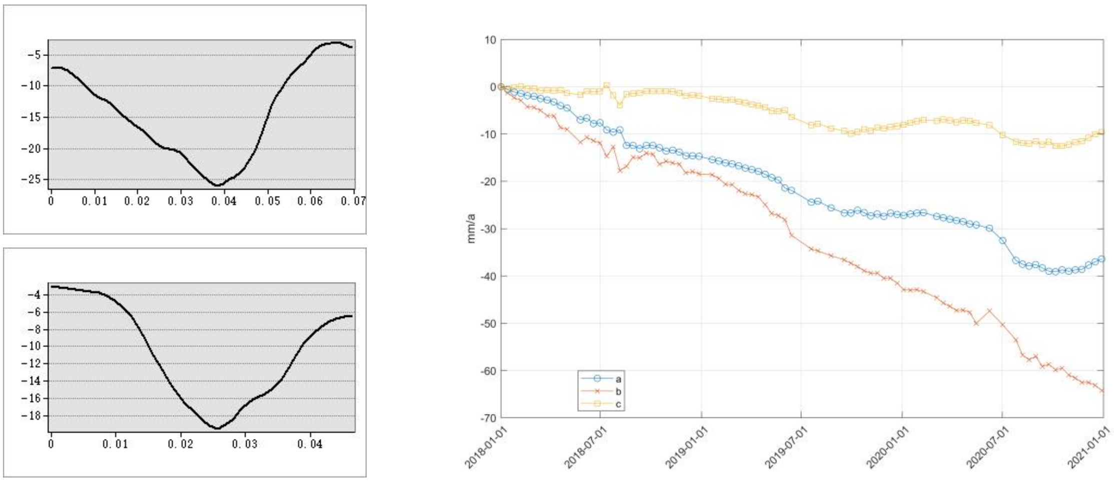

Figure 15. The upper left represents L1, and the lower left represents L2. The right side shows the subsidence time series curves for randomly selected points.

The cross-sectional analysis of the two regions in Yangcheng County shows similar subsidence trends in Figure 15. Region 1 initially shows subsidence of about 7 mm, increasing with distance, reaching a maximum of -25 mm/year at 0.04 degrees, and then stabilizing. Region 2 shows a similar trend, with a maximum subsidence rate of -20 mm/year. These subsidence patterns exhibit a funnel shape, common to mining areas.

As shown in Figure 14, For the three monitoring points in the small mining area clusters of Yangcheng County, all points show a downward trend, indicating subsidence. Point c shows the least subsidence, only 10 mm over three years. Point b shows the fastest subsidence, with a linear trend reaching 65 mm by December 2020. The subsidence map indicates that point b is located at the center of a mining area, experiencing severe subsidence. Point a shows moderate subsidence, initially stable but with a significant drop from 30 mm to 40 mm in July 2020, after which it stabilizes.

4.4 LSTM Model Prediction

Merely relying on obtained subsidence information does not meet the demands of monitoring subsidence in mining areas. We randomly selected time series subsidence values from mining area clusters in Jincheng City and used GRU, VMD-GRU, and VMD-GRU-LSTM models to predict future time series data. Root Mean Square Error (RMSE), Mean Absolute Error (MAE), and Mean Absolute Percentage Error (MAPE) were used to compare and evaluate different prediction models, and the optimal model was chosen to meet the needs of subsidence prevention in subway construction.

4.4.1 Variational Mode Decomposition Results

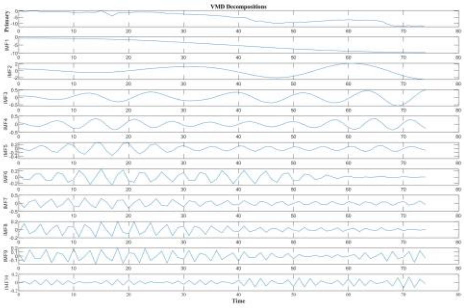

Figure 16. VMD Layer-by-Layer Decomposition Process

VMD, as a powerful time-frequency analysis tool, reveals the multi-level intrinsic structure of the original signal through layer-by-layer decomposition, as shown in Figure16. The original time series signal is decomposed into ten Intrinsic Mode Functions (IMFs), each representing different frequency components within the signal. Specifically, IMF1 has the lowest frequency, revealing the slowest trend changes in the signal, while IMF10 has the highest frequency, capturing rapid changes and detailed features. IMFs 1 to 2 show the low-frequency components of the signal, corresponding to the overall trend and slow changes. IMFs 3 to 6 mainly reflect the medium-frequency components, revealing periodic fluctuations and smoother wave patterns. IMFs 7 to 10 present high-frequency components, capturing high-frequency details and noise in the signal. Through VMD decomposition, we can more clearly understand and analyze the various frequency components in the original time series signal, providing a basis for subsequent model predictions.

4.4.2 Time Series Prediction Model Comparison and Analysis

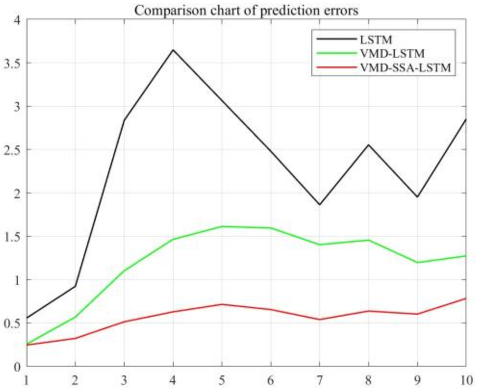

Figure 17. Comparison of Prediction Errors of Different Models on the Test Set

We tested the single LSTM model and the VMD-LSTM and VMD-SSA-LSTM models. Each curve represents a model, with the horizontal axis indicating sample index and the vertical axis indicating the prediction error magnitude. The Figure17 shows that the single LSTM model's error curve fluctuates the most, indicating instability. The best prediction model is the VMD-SSA-LSTM model, with a maximum prediction error of no more than 1 mm compared to the true values and relatively stable performance. Although the VMD-LSTM model also performs well, its accuracy is lower than that of the VMD-SSA-LSTM model.

We quantified the errors for analysis: on the training set, the VMD-LSTM model has an RMSE of 0.56949, an MAE of 0.46604, and a MAPE of 17.103%. On the test set, its RMSE is 1.2665, MAE is 1.193, and MAPE is 10.9131%. In contrast, the VMD-SSA-LSTM model shows lower RMSE (0.097174), MAE (0.07103), and MAPE (4.5414%) on the training set, and maintains relatively low error metrics on the test set with an RMSE of 0.58664, an MAE of 0.5647, and a MAPE of 5.2252%. These results indicate that the VMD-SSA-LSTM model achieves better performance on both the training and test sets, with lower prediction errors and higher accuracy, making it more suitable for the prediction task.

4.4.3 Comparison and Analysis of Time Series Prediction Results

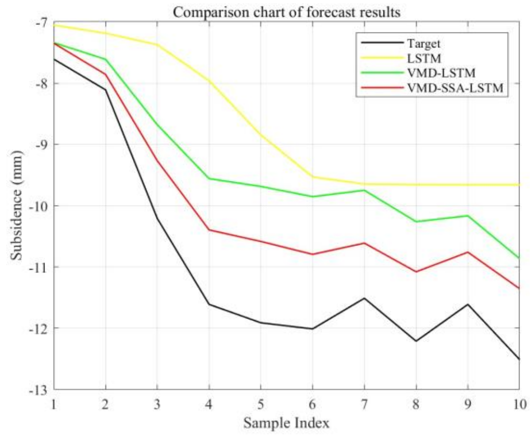

Figure 18. Comparison of Prediction Results of Different Models

Figure 18 compares the subsidence data predictions of four models: Target (actual values), LSTM, VMD-LSTM, and VMD-SSA-LSTM. The vertical axis represents subsidence (in mm) and the horizontal axis represents sample index. It is evident that the VMD-SSA-LSTM model has the best predictive performance.

Specifically, the target value curve (black) represents the actual subsidence data, used to evaluate the accuracy of each prediction model. The LSTM model's prediction curve (yellow) deviates significantly from the actual values between sample indices 3 and 6, indicating noticeable prediction errors and inadequacies in handling complex subsidence data changes. The VMD-LSTM model's prediction curve (green) shows significant improvement over the pure LSTM model, with overall reduced prediction errors, but still exhibits larger deviations at sample indices 9 and 10, indicating local prediction inaccuracies.

Notably, the VMD-SSA-LSTM model's prediction curve (red) demonstrates higher accuracy at each sample point. By first using VMD to decompose the signal, then applying SSA to remove noise, and finally using LSTM for prediction, this model effectively captures the complex patterns and trends in subsidence data. Consequently, its prediction results are very close to the actual values at most sample points, with minimal errors, indicating the best performance.

In summary, the VMD-SSA-LSTM model excels in predicting subsidence data, outperforming other models. This superior performance is attributed to its comprehensive use of VMD for signal feature decomposition, SSA for data smoothing, and LSTM for time series prediction, enabling more accurate reflection of real subsidence data changes.

5 Discussion

The formation of mining area clusters in Jincheng City can be attributed to a series of interacting driving factors, including changes in land use patterns, large-scale mining activities, changes in groundwater reserves, and geological structures. The surface and subsurface deformations caused by these factors have profound impacts on the economic construction and social development of Jincheng City.

5.1 Land Use Changes

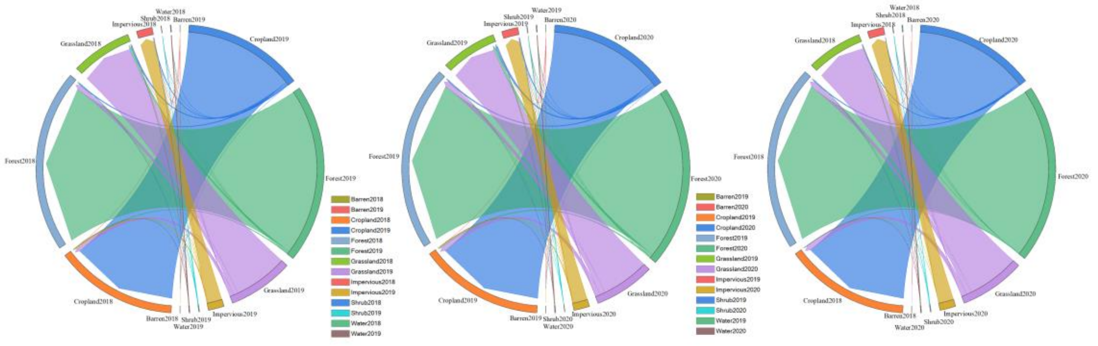

Figure 19. Land Use Changes in Jincheng City

Changes in land use data reflect the redistribution of land resources and shifts in utilization methods within the region. These changes mainly affect the geological stability and deformation processes of mining areas by altering the physical and chemical environment of the surface and subsurface[36,37]. As shown in Figure 19, From 2018 to 2020, significant changes in land use types occurred in Jincheng City, greatly influencing mining area deformations[38,39]. Farmland primarily transformed into impervious surfaces and grassland, approximately 92.41 square kilometers, increasing surface runoff and reducing groundwater recharge, potentially leading to surface subsidence. Forest area increased by 148.45 square kilometers from 2018 to 2020, which helps stabilize the soil and reduce erosion and geological deformation, but requires comprehensive consideration of impacts on groundwater and geological structure. Frequent transitions between grassland and farmland indicate instability in land use, increasing the risk of geological deformation. Impervious surface area increased from 391.73 square kilometers in 2018 to 403.50 in 2020, an increase of 11.77 square kilometers, potentially triggering local geological disasters such as surface subsidence and landslides[40]. Therefore, rational planning of land use, controlling urbanization processes, protecting and restoring vegetation cover, and scientifically managing groundwater resources are key measures to reduce geological disasters and ensure the geological stability of mining areas and their surroundings[41,42].

5.2 Geological Structure

The geological structure of Jincheng City is primarily composed of carbonate rocks and sedimentary rocks, including limestone and dolomite. These rocks are prone to dissolution, forming developed karst fracture systems. Particularly during large-scale mining development, mining activities exacerbate the expansion and deepening of geological fractures[43,44]. Limestone and dolomite tend to form wide and penetrating fractures under stress, further increasing the risk of geological deformation[45]. Geological deformation in mining areas can lead to surface subsidence, ground fissures, and other geological disasters, damaging surface structures and affecting groundwater systems, thereby negatively impacting regional economic construction and social development. The development of geological fractures can also result in groundwater loss and resource pollution, exacerbating geological and environmental problems in mining areas and their surroundings[46]. The formation of mining area clusters in Jincheng City is partly due to its unique geological structure. Reasonable planning of mining development and geological exploration, as well as the protection and management of groundwater resources, are beneficial for preventing geological disasters and ensuring mining area stability.

5.3 Large-Scale Mining Activities

Large-scale mining activities have multifaceted impacts on mining area deformation. Firstly, large-scale mining, especially underground mining, creates significant voids within the rock mass. These man-made spaces disrupt the original rock stress field balance in the mining strata, directly causing mining area deformation[47,48]. Secondly, although mining-induced tectonic stress has localized distribution characteristics, its strong force significantly exacerbates mining area deformation. With increasing mining depth and scale, factors such as groundwater level decline, groundwater drainage, and rock mass loosening also affect the geological structure of mining areas, further impacting deformation[49]. Additionally, mining activities can trigger geological disasters such as earthquakes and geological liquefaction, increasing deformation severity. Moreover, topographic and geomorphological factors such as slope, aspect, terrain undulation, and surface incision depth may also become important factors influencing deformation during mining development[50]. These factors interact with mining activities, collectively constituting the complex mechanism of mining area deformation.

5.4 Changes in Groundwater Reserves

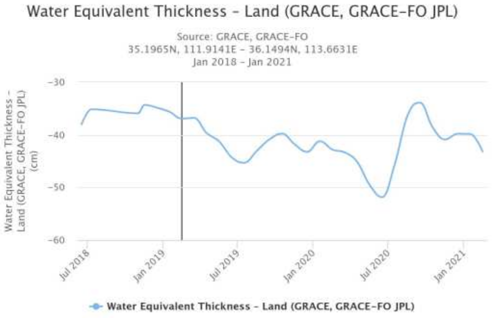

Figure 20 Temporal Changes in Terrestrial Water Equivalent Thickness in Jincheng City

Generally, changes in groundwater reserves directly affect surface subsidence. As shown in Figure 20, We selected the terrestrial water equivalent thickness changes in Jincheng City observed by GRACE and GRACE-FO satellites[51,52] from January 2018 to January 2021. Overall, the trend indicates a decline in water equivalent thickness during this period, suggesting reduced water storage in the area. The data shows clear seasonal fluctuations, with periodic increases and decreases approximately every year, likely related to precipitation, evaporation, and snowmelt[51,53]. Significant peaks occurred in mid-2018 and early 2020, while troughs appeared in mid-2019 and mid-2020. The overall fluctuation range is between -30 cm and -55 cm, with the maximum negative value at the end of the period, indicating significant water storage reduction. This change could be influenced by climatic variations, changes in land use, or other environmental factors. In comparison with the subsidence trend in the large-scale cluster in Jincheng City, the correlation between the two trends is not significant, suggesting a minor impact of water storage on subsidence in mining areas, which can be considered negligible.

6 Conclusion

This study combines time-series InSAR (TS-InSAR) technology, analysis of land use change, and a multivariate neural network prediction model to propose a comprehensive method for analyzing surface deformation and land use change in the large-scale mining area of Jincheng City. The TS-InSAR method effectively monitors surface deformation with high precision, revealing dynamic changes in deformation areas. The subsidence rate in Jincheng City ranged from -34 mm to 34 mm per year from January 2018 to January 2021. By dividing the large-scale mining cluster into four different regions for analysis, the results show slight differences in subsidence among different areas. The maximum subsidence area is located in Gaoping City at -34.08 mm per year, while the largest variation in subsidence occurs in Yangcheng County, ranging from -28 mm to -25 mm per year, with a maximum difference of 51 mm per year between the highest and lowest subsidence values. However, each area shares common characteristics, with maximum subsidence determined by small clusters of mining areas. These areas interact with each other and eventually evolve into the large-scale cluster observed in Jincheng City. Finally, through a series of subsidence data in Jincheng City, the optimal VMD-SSA-LSTM mining subsidence prediction model was obtained. This model not only demonstrates lower RMSE (0.097174) and MAE (0.07103) on the training set but also maintains relatively lower RMSE of 0.58664 and MAE of 0.5647 on the test set. Analysis indicates that the formation of large-scale mining area clusters is influenced by three typical factors: mining activities, changes in land use, and geological structures. Future work requires gathering detailed on-site information to assist in research on mining deformation and risk assessment of various deformation patterns based on deep learning methods.

Data availability

The data presented in the study are available on request from the first and corresponding author. The data are not publicly available due to the thesis that is being prepared from these data.

Reference

1. Düzgün, Ş.; Künzer, C.; Özgen Karacan, C. Applications of Remote Sensing and GIS for Monitoring of Coal Fires, Mine Subsidence, Environmental Impacts of Coal-Mine Closure and Reclamation. *Int. J. Coal Geol.* **2011**, *86*, 1–2, doi:10.1016/j.coal.2011.02.001.
2. Kumari, M.; Bhattacharya, T. A Review on Bioaccessibility and the Associated Health Risks Due to Heavy Metal Pollution in Coal Mines: Content and Trend Analysis. *Environ. Dev.* **2023**, 100859.
3. Wang, Y.; Zhang, Y. Study on Optimization of Layout Parameters of High-Level Boreholes in Pingdingshan Coal Mine. *Sci. Rep.* **2023**, *13*, 19759.
4. Xu, K.; Li, S.; Liu, J.; Lu, C.; Xue, G.; Xu, Z.; He, C. Evaluation Cloud Model of Spontaneous Combustion Fire Risk in Coal Mines by Fusing Interval Gray Number and DEMATEL. *Sustainability* **2022**, *14*, 15585, doi:10.3390/su142315585.
5. Xu, X.; Zhao, D.; Ma, C.; Lian, D. Monitoring Subsidence Deformation of Suzhou Subway Using InSAR Timeseries Analysis. *IEEE Access* **2021**, *9*, 3400–3416, doi:10.1109/ACCESS.2020.3047574.
6. Zhang, J.; Ke, C.; Shen, X.; Lin, J.; Wang, R. Monitoring Land Subsidence along the Subways in Shanghai on the Basis of Time-Series InSAR. *Remote Sens.* **2023**, *15*, 908, doi:10.3390/rs15040908.
7. Cai, J.; Zhang, L.; Dong, J.; Guo, J.; Wang, Y.; Liao, M. Automatic Identification of Active Landslides over Wide Areas from Time-Series InSAR Measurements Using Faster RCNN. *Int. J. Appl. Earth Obs. Geoinformation* **2023**, *124*, 103516, doi:10.1016/j.jag.2023.103516.
8. Dai, K.; Chen, C.; Shi, X.; Wu, M.; Feng, W.; Xu, Q.; Liang, R.; Zhuo, G.; Li, Z. Dynamic Landslides Susceptibility Evaluation in Baihetan Dam Area during Extensive Impoundment by Integrating Geological Model and InSAR Observations. *Int. J. Appl. Earth Obs. Geoinformation* **2023**, *116*, 103157, doi:10.1016/j.jag.2022.103157.
9. Guo, H.; Yuan, Y.; Wang, J.; Cui, J.; Zhang, D.; Zhang, R.; Cao, Q.; Li, J.; Dai, W.; Bao, H.; et al. Large-Scale Land Subsidence Monitoring and Prediction Based on SBAS-InSAR Technology with Time-Series Sentinel-1A Satellite Data. *Remote Sens.* **2023**, *15*, 2843, doi:10.3390/rs15112843.
10. An, B.; Jiang, Y.; Wang, C.; Shen, P.; Song, T.; Hu, C.; Liu, K. Ground Infrastructure Monitoring in Coastal Areas Using Time-Series inSAR Technology: The Case Study of Pudong International Airport, Shanghai. *Int. J. Digit. Earth* **2023**, *16*, 355–374, doi:10.1080/17538947.2023.2171144.
11. Chen Y.; He Y.; Zhang L.; Chen B.; He X.; Pu H.; Cao S.; Gao L.; Yang W.; Faculty of Geomatics, Lanzhou Jiaotong University, Lanzhou 730070, China; et al. Surface deformation prediction based on TS-InSAR technology and long short-term memory networks. *Natl. Remote Sens. Bull.* **2022**, *26*, 1326–1341, doi:10.11834/jrs.20221457.
12. Deng, Z.; Ke, Y.; Gong, H.; Li, X.; Li, Z. Land Subsidence Prediction in Beijing Based on PS-InSAR Technique and Improved Grey-Markov Model. *GIScience Remote Sens.* **2017**, *54*, 797–818, doi:10.1080/15481603.2017.1331511.
13. Zhang, Z.; Hu, C.; Wu, Z.; Zhang, Z.; Yang, S.; Yang, W. Monitoring and Analysis of Ground Subsidence in Shanghai Based on PS-InSAR and SBAS-InSAR Technologies. *Sci. Rep.* **2023**, *13*, 8031, doi:10.1038/s41598-023-35152-1.
14. Li, T.; Zhang, H.; Fan, H.; Zheng, C.; Liu, J. Position Inversion of Goafs in Deep Coal Seams Based on DS-InSAR Data and the Probability Integral Methods. *Remote Sens.* **2021**, *13*, 2898, doi:10.3390/rs13152898.
15. Zhang, L.; Gao, P.; Gan, Z.; Wu, W.; Sun, Y.; Zhu, C.; Long, S.; Liu, M.; Peng, H. Surface Subsidence Monitoring of Mining Areas in Hunan Province Based on Sentinel-1A and DS-InSAR. *Sensors* **2023**, *23*, 8146, doi:10.3390/s23198146.
16. Mason, P.J.; Bischoff, C.A.; Hughes, G.; Petrone, C.M.; Varley, N.R.; Nicholas, G.; Ferretti, A. Monitoring Ground Movement at Volcán de Colima, Mexico, Using Sentinel-1 Data and SqueeSAR ®. *Q. J. Eng. Geol. Hydrogeol.* **2023**, *56*, qjegh2022-047, doi:10.1144/qjegh2022-047.
17. Bischoff, C.A.; Ferretti, A.; Novali, F.; Uttini, A.; Giannico, C.; Meloni, F. Nationwide Deformation Monitoring with SqueeSAR® Using Sentinel-1 Data. *Proc. Int. Assoc. Hydrol. Sci.* **2020**, *382*, 31–37, doi:10.5194/piahs-382-31-2020.
18. Shi, W.; Chen, G.; Meng, X.; Jiang, W.; Chong, Y.; Zhang, Y.; Dong, Y.; Zhang, M. Spatial-Temporal Evolution

of Land Subsidence and Rebound over Xi'an in Western China Revealed by SBAS-InSAR Analysis. *Remote Sens.* **2020**, *12*, 3756, doi:10.3390/rs12223756.

19. Liu, Y.; Zhang, J. Integrating SBAS-InSAR and AT-LSTM for Time-Series Analysis and Prediction Method of Ground Subsidence in Mining Areas. *Remote Sens.* **2023**, *15*, 3409, doi:10.3390/rs15133409.

20. Howe, L.; Johnston, S.; Côte, C. Mining-Related Environmental Disasters: A High Reliability Organisation (HRO) Perspective. *J. Clean. Prod.* **2023**, *417*, 137965, doi:10.1016/j.jclepro.2023.137965.

21. Owen, J.R.; Kemp, D.; Lèbre, É.; Svobodova, K.; Pérez Murillo, G. Catastrophic Tailings Dam Failures and Disaster Risk Disclosure. *Int. J. Disaster Risk Reduct.* **2020**, *42*, 101361, doi:10.1016/j.ijdrr.2019.101361.

22. Giurco, D.; Cooper, C. Mining and Sustainability: Asking the Right Questions. *Miner. Eng.* **2012**, *29*, 3–12, doi:10.1016/j.mineng.2012.01.006.

23. Asr, E.T.; Kakaie, R.; Ataei, M.; Tavakoli Mohammadi, M.R. A Review of Studies on Sustainable Development in Mining Life Cycle. *J. Clean. Prod.* **2019**, *229*, 213–231, doi:10.1016/j.jclepro.2019.05.029.

24. Mudd, G.M. Global Trends in Gold Mining: Towards Quantifying Environmental and Resource Sustainability. *Resour. Policy* **2007**, *32*, 42–56, doi:10.1016/j.resourpol.2007.05.002.

25. Zhang, B.; Liao, X.; Zhang, J.; Xiong, S.; Wang, C.; Wu, S.; Zhu, C.; Zhu, J.; Qin, X.; Li, Q. Megalopolitan-Scale Ground Deformation along Metro Lines in the Guangdong-Hong Kong-Macao Greater Bay Area, China, Revealed by MT-InSAR. *Int. J. Appl. Earth Obs. Geoinformation* **2023**, *122*, 103432, doi:10.1016/j.jag.2023.103432.

26. Yu, W.; Gong, H.; Chen, B.; Zhou, C.; Zhang, Q. Combined GRACE and MT-InSAR to Assess the Relationship between Groundwater Storage Change and Land Subsidence in the Beijing-Tianjin-Hebei Region. *Remote Sens.* **2021**, *13*, 3773, doi:10.3390/rs13183773.

27. Ding, L.; Li, C.; Lei, Z.; Zhang, C.; Wei, L.; Guo, Z.; Li, Y.; Fan, X.; Qi, D.; Wang, J. Spatiotemporal Evolution of Deformation and LSTM Prediction Model over the Slope of the Deep Excavation Section at the Head of the South-North Water Transfer Middle Route Canal. *Heliyon* **2024**, *10*, e26301, doi:10.1016/j.heliyon.2024.e26301.

28. Ma, F.; Sui, L.; Lian, W. Prediction of Mine Subsidence Based on InSAR Technology and the LSTM Algorithm: A Case Study of the Shigouyi Coalfield, Ningxia (China). *Remote Sens.* **2023**, *15*, 2755, doi:10.3390/rs15112755.

29. Li, S.; Dong, B.; Gao, X.; Xu, H.; Ren, C.; Liu, Y.; Peng, L. Study on Spatio-Temporal Evolution of Habitat Quality Based on Land-Use Change in Chongming Dongtan, China. *Environ. Earth Sci.* **2022**, *81*, 220, doi:10.1007/s12665-022-10324-w.

30. Liu, Y.; Zhang, J. Integrating SBAS-InSAR and AT-LSTM for Time-Series Analysis and Prediction Method of Ground Subsidence in Mining Areas. *Remote Sens.* **2023**, *15*, 3409, doi:10.3390/rs15133409.

31. Fang, M.; Zhang, F.; Cao, Z.; Tao, R.; Xiao, W.; Zhu, D.; Gui, Z.; Xiao, R. Prediction Accuracy Improvement of Pressure Pulsation Signals of Reversible Pump-turbine: A LSTM and VMD-based Optimization Approach. *Energy Sci. Eng.* **2024**, *12*, 102–116, doi:10.1002/ese3.1620.

32. Guo, F.; Deng, S.; Zheng, W.; Wen, A.; Du, J.; Huang, G.; Wang, R. Short-Term Electricity Price Forecasting Based on the Two-Layer VMD Decomposition Technique and SSA-LSTM. *Energies* **2022**, *15*, 8445, doi:10.3390/en15228445.

33. Kalavrezou, I.-E.; Castro-Melgar, I.; Nika, D.; Gatsios, T.; Lalechos, S.; Parcharidis, I. Application of Time Series INSAR (SBAS) Method Using Sentinel-1 for Monitoring Ground Deformation of the Aegina Island (Western Edge of Hellenic Volcanic Arc). *Land* **2024**, *13*, 485, doi:10.3390/land13040485.

34. Wu, Z.; Ma, P.; Zheng, Y.; Gu, F.; Liu, L.; Lin, H. Automatic Detection and Classification of Land Subsidence in Deltaic Metropolitan Areas Using Distributed Scatterer InSAR and Oriented R-CNN. *Remote Sens. Environ.* **2023**, *290*, 113545, doi:10.1016/j.rse.2023.113545.

35. Keren, G.; Schuller, B. Convolutional RNN: An Enhanced Model for Extracting Features from Sequential Data 2017.

36. Zhao, L.; Su, M.; Wang, X.; Li, X.; Chang, X.; Zhang, P. Spatial–Temporal Evolution and Prediction of Habitat

Quality in Beijing–Tianjin–Hebei Region Based on Land Use Change. *Land* **2023**, *12*, 667.

37. Su, J.; Zhang, R.; Wu, M.; Yang, R.; Liu, Z.; Xu, X. Correlation between Spatial-Temporal Changes in Landscape Patterns and Habitat Quality in the Yongding River Floodplain, China. *Land* **2023**, *12*, 807.

38. Peng, C.; Wang, Y.; Dong, J.; Huang, C. Impact of Land Use Change on the Habitat Quality Evolution in Three Gorges Reservoir Area, China. *Int. J. Environ. Res. Public. Health* **2023**, *20*, 3138.

39. Li, T.; Bao, R.; Li, L.; Tang, M.; Deng, H. Temporal and Spatial Changes of Habitat Quality and Their Potential Driving Factors in Southwest China. *Land* **2023**, *12*, 346.

40. Nardini, O.; Confuorto, P.; Intrieri, E.; Montalti, R.; Montanaro, T.; Robles, J.G.; Poggi, F.; Raspini, F. Integration of Satellite SAR and Optical Acquisitions for the Characterization of the Lake Sarez Landslides in Tajikistan. *Landslides* **2024**, *21*, 1385–1401, doi:10.1007/s10346-024-02214-y.

41. Alshehri, F.; Mohamed, A. Analysis of Groundwater Storage Fluctuations Using GRACE and Remote Sensing Data in Wadi As-Sirhan, Northern Saudi Arabia. *Water* **2023**, *15*, 282, doi:10.3390/w15020282.

42. Hakim, W.L.; Fadhillah, M.F.; Lee, K.-J.; Lee, S.-J.; Chae, S.-H.; Lee, C.-W. Land Subsidence and Groundwater Storage Assessment Using ICOPS, GRACE, and Susceptibility Mapping in Pekalongan, Indonesia. *IEEE Trans. Geosci. Remote Sens.* **2023**, *61*, 1–25, doi:10.1109/TGRS.2023.3324043.

43. Stern, R.J. The Evolution of Plate Tectonics. *Philos. Trans. R. Soc. Math. Phys. Eng. Sci.* **2018**, *376*, 20170406, doi:10.1098/rsta.2017.0406.

44. Gorbushina, A.A. Life on the Rocks. *Environ. Microbiol.* **2007**, *9*, 1613–1631, doi:10.1111/j.1462-2920.2007.01301.x.

45. Zheng, Y.-F.; Xiao, W.-J.; Zhao, G. Introduction to Tectonics of China. *Gondwana Res.* **2013**, *23*, 1189–1206, doi:10.1016/j.gr.2012.10.001.

46. Deprez, M.; De Kock, T.; De Schutter, G.; Cnudde, V. A Review on Freeze-Thaw Action and Weathering of Rocks. *Earth-Sci. Rev.* **2020**, *203*, 103143, doi:10.1016/j.earscirev.2020.103143.

47. Ma, D.; Zhao, R.; Li, Y.; Li, Z. Land Subsidence Assessment of an Archipelago Based on the InSAR Time Series Analysis Method. *Water* **2023**, *15*, 465, doi:10.3390/w15030465.

48. Umarhadi, D.A.; Widyatmanti, W.; Kumar, P.; Yunus, A.P.; Khedher, K.M.; Kharrazi, A.; Avtar, R. Tropical Peat Subsidence Rates Are Related to Decadal LULC Changes: Insights from InSAR Analysis. *Sci. Total Environ.* **2022**, *816*, 151561, doi:10.1016/j.scitotenv.2021.151561.

49. Kabiesz, J.; Lurka, A.; Drzewiecki, J. Selected Methods of Rock Structure Disintegration to Control Mining Hazards / Wybrane Metody Dezintegracji Struktury Skał Dla Zwalczania Zagrożeń Górniczych. *Arch. Min. Sci.* **2015**, *60*, 807–824, doi:10.1515/amsc-2015-0053.

50. Kim, J.; Lin, S.-Y.; Singh, T.; Singh, R.P. InSAR Time Series Analysis to Evaluate Subsidence Risk of Monumental Chandigarh City (India) and Surroundings. *IEEE Trans. Geosci. Remote Sens.* **2023**, *61*, 1–15, doi:10.1109/TGRS.2023.3305863.

51. Syed, T.H.; Famiglietti, J.S.; Rodell, M.; Chen, J.; Wilson, C.R. Analysis of Terrestrial Water Storage Changes from GRACE and GLDAS. *Water Resour. Res.* **2008**, *44*, 2006WR005779, doi:10.1029/2006WR005779.

52. Massoud, E.C.; Liu, Z.; Shaban, A.; Hage, M. Groundwater Depletion Signals in the Beqaa Plain, Lebanon: Evidence from GRACE and Sentinel-1 Data. *Remote Sens.* **2021**, *13*, 915, doi:10.3390/rs13050915.

53. Hakim, W.L.; Nur, A.S.; Rezaie, F.; Panahi, M.; Lee, C.-W.; Lee, S. Convolutional Neural Network and Long Short-Term Memory Algorithms for Groundwater Potential Mapping in Anseong, South Korea. *J. Hydrol. Reg. Stud.* **2022**, *39*, 100990, doi:10.1016/j.ejrh.2022.100990.